3

Anisotropic Second- and Third-Order Nonlinear Optical Response from Anisotropy-Controlled Metallic Nanocomposites

Roberto-Carlos Fernández-Hernández[1], Lis Tamayo-Rivera[1],
Israel Rocha-Mendoza[2], Raúl Rangel-Rojo[2],
Alicia Oliver[1] and Jorge-Alejandro Reyes-Esqueda[1]
[1]*Institute of Physics, National Autonomous University of Mexico, Circuit for Scientific Research S/N, University City, Mexico City,*
[2]*Department of Optics, Center for Scientific Research and Education Superior de Ensenada, Ensenada, Mexico*

1. Introduction

Plasmonics has become a route to develop ultracompact optical devices on a chip by using extreme light concentration. It also gives the ability to perform simultaneous electrical and optical functions, and facilitates dramatic enhancement of localized field intensities via metallic nanostructures. On the other hand, nonlinear optical interactions scale with the local intensity of the optical field, i.e., the dielectric polarization of a given material responds to the local electric field in a high-order way. For a metal-dielectric nanostructure, the combination of plasmonics with its nonlinear optical response offers the opportunity to manipulate nonlinear optical responses in sub-diffraction-limited volumes.

Nevertheless, before taking advantage of such opportunity, a strong understanding of the nonlinear optical response due to metallic nanoparticles is necessary (Fernández-Hernández et al., 2011; Rangel-Rojo et al., 2009, 2010; Reyes-Esqueda et al., 2009; Rodríguez-Iglesias et al., 2009; Torres-Torres et al., 2008). On doing so, the possibility of conferring anisotropic symmetries to metallic nanocomposites (Oliver et al., 2006; Rodríguez-Iglesias et al., 2008; Silva-Pereyra et al., 2010) revealed also the anisotropy of their linear and nonlinear optical responses (Fernández-Hernández et al., 2011; Rangel-Rojo et al., 2009, 2010; Reyes-Esqueda et al., 2008, 2009; Rodríguez-Iglesias et al., 2009). In particular, the anisotropic nonlinear optical response, for given wavelength and incident polarization, reveals a complex contribution from all the different, nonzero, linearly independent third-order susceptibility tensor's components (Reyes-Esqueda et al., 2009; Rodríguez-Iglesias et al., 2009). Besides, given this anisotropy, although the nanocomposite remains being centrosymmetric, there is the possibility of measuring a nonzero optical second-order nonlinearity in the form of a second harmonic generation (SHG) signal, as it has been shown in previous results (Aktsipetrov et al., 1995; Brevet et al., 2011; Dadap et al., 1999, 2004; Figliozze et al., 2005; Gallet et al., 2003; Mendoza et al., 2006), and also verified by us experimentally (Rocha-Mendoza et al., 2011).

Therefore, in this chapter we first present an overview of recent studies about the nonlinear optical response of metallic nanoparticles. Then, we present recent previous results regarding the third-order nonlinear optical response of metallic nanocomposites. After that, we discuss the dependence of this response on the tensor's components, making emphasis on the anisotropic case. Finally, we calculate the general form of the second-order susceptibility tensor for anisotropic nanocomposites, together with some experimental results for the polarization dependence of second harmonic generation in these composites.

2. Nonlinear optical response of metallic nanoparticles

In recent years, nanostructured materials composed of metal nanoparticles (NPs) have attracted much attention due to the possibility of using their nonlinear optical properties for photonic nanodevices (Inouye et al., 2000; Matsui, 2005) and plasmonic circuitry (Barnes et al., 2003; Tominaga et al., 2001). Their linear and nonlinear optical properties are dominated by collective electron-plasma oscillations, the so-called localized surface plasmon resonances (LSPRs), and a vast literature can be found elsewhere studying such properties (Aktsipetrov et al., 1995; Barnes et al., 2003; Brevet, 2011; Dadap et al., 1999; Inouye et al., 2000; Karthikeyan et al., 2008; Kim et al., 2006; Matsui, 2005; McMahon et al., 2007; Rangel-Rojo et al., 2009, 2010; Ryasnyansky et al., 2006; Tominaga et al., 2001; Zheludev & Emelyanov, 2004). In particular, in 2008, when studying Cu NPs embedded in a silica matrix using nanosecond and picosecond light pulses, we found that thermal effects for the nanosecond regime, and induced polarization for the picosecond one, were the physical mechanisms responsible for the saturable optical absorption and the Kerr effect presented by the nanocomposites (Torres-Torres et al., 2008). However, by following Hache, *et al.* (Hache et al., 2004), we also remarked the contribution of the hot-electrons generation to the observation of saturable absorption. From there, we have widely studied the optical third-order nonlinearity of randomly arranged, but elongated and aligned in a preferential direction, metallic NPs embedded in silica (Fernández-Hernández et al., 2011; Rangel-Rojo et al., 2009, 2010; Reyes-Esqueda et al., 2009; Rodríguez-Iglesias et al., 2009). We have put especial attention, on one hand, to the contribution to these properties from the electron transitions charactheristic of metallic NPs, that is, intra- and inter-band transitions, but also to the contribution from the mentioned hot-electrons generation (Fernández-Hernández et al., 2011). From here, the dependence of these nonlinearities on the incident wavelength and irradiance has been observed, allowing also the observation of sign switching of the nonlinear absorption and refraction (Fernández-Hernández et al., 2011). On the other hand, the shape-anisotropy of the ion-deformed metallic NPs embedded in a dielectric matrix (Oliver et al., 2006; Rodríguez-Iglesias et al., 2008; Silva-Pereyra et al., 2010) induces also an anisotropic third-order nonlinear optical response, as we have shown for different temporal regimes, in the case of Ag and Au (Fernández-Hernández et al., 2011; Rangel-Rojo et al., 2009; Reyes-Esqueda et al., 2009; Rodríguez-Iglesias et al., 2009). For the anisotropic nanocomposites the analysis is now more complex: there are two LSPRs, one associated to the major axis of the elongated NP, and another one associated to its minor axis. This fact duplicates the contribution from the intra-band transitions, but also that from the hot-electrons generation. Besides, the form of the nonlinear susceptibility tensor becomes very specific, having now only three linearly independent, nonzero components (Reyes-Esqueda

et al., 2009; Rodríguez-Iglesias et al., 2009), where each one of them may be measured depending on the incident polarization of the exciting beam, and on the angular position of the nanocomposite with respect to the beam's wavevector. We have shown also the possibility of understanding the nonlinear optical absorption behavior by using a two-level model (Rangel-Rojo et al., 2009). Thus, for the third-order nonlinear optical response from isotropic and anisotropic metallic NPs, besides of being very large, the sign of both the nonlinear absorption and refraction can change, depending on the wavelength, irradiance and incident polarization (Fernández-Hernández et al., 2011).

Regarding the second-order nonlinear optical response, metallic NPs are centrosymmetrical materials, their crystalline lattice structures are cubic face-centered and, in principle, no SHG from the bulk NP takes place in the electric dipole approximation. The SHG origin of such materials is attributed then to higher order interactions like electric quadrupole and magnetic dipole responses from the NPs bulk and/or electric dipole responses allowed from the NPs surfaces (Aktsipetrov et al., 1995; Brevet et al., 2011; Dadap et al., 1999, 2004; Figliozze et al., 2005; Gallet et al., 2003; Mendoza et al., 2006), where the inversion symmetry of the bulk material is broken. The latter response dominates in the specific case when the NP size is much smaller than the wavelength of the exciting (fundamental) beam (Aktsipetrov et al., 1995) so that field retardation effects (no spatial dependence of the electromagnetic fields) are neglected. Therefore, the problem at the macroscopic level turns to be very similar to that of nonlinear media containing particles of non-centrosymmetrical material apart from the interfacial second-order origin of the response. In a sense, the arrangement of the NPs in the array resembles that of the atoms in a crystal cell, where phase-matched SHG signal radiates in specific directions. This principle has been utilized for example on planar structures containing metallic 2D arrays of nanoparticles lacking inversion symmetry, providing coherent addition of the SH field where the efficiency of the process increased rapidly with decreasing nanoparticle size (McMahon et al., 2007; Zheludev et al., 2004). In this context, we demonstrate that, similar to the analysis to derive molecular orientation information of smaller noncentrosymmetic units at interfacial monolayer's or macromolecules systems using SHG/Sum-Frequency Generation (SFG) experiments (Knoesen et al., 2004; Leray et al., 2004; Psilodimitrakopoulos et al., 2009; Campagnola & Loew, 2003; Rocha-Mendoza et al., 2007; Shen, 1989; Zhuang et al., 1999), we can treat the actual submicrometric layer containing randomly arranged, but highly aligned anisotropically shaped Ag-NPs (elongated or nearly spherical), as a nonlinear media; where the origin of its macromolecular second-order susceptibility, $\chi^{(2)}$, is the coherent contribution of the SH signal induced on every single nanoparticle.

3. Third-order nonlinear optical response from isotropic metallic nanocomposites

In order to get more control of the nonlinear optical response from metallic nanocomposites, very recently we carefully studied the wavelength dependence of this response (Fernández-Hernández et al., 2011). To do that, we performed closed- and open-aperture Z-scan measurements at several wavelengths in isotropic and anisotropic metallic nanocomposites produced by ion implantation. We have observed dramatic changes of sign for both

nonlinear refraction and absorption, when passing from Au to Ag and/or varying the wavelength and irradiance. The results put into evidence the hot-electron contribution to the nonlinear optical response, when compared to inter- and intra-band transitions contribution. In this section, we present the main results obtained concerning the isotropic nanocomposites, leaving those from the anisotropic ones for the next section.

3.1 Synthesis of isotropic metallic nanocomposites and optical measurements

As reported before (Oliver et al., 2006; Reyes-Esqueda et al., 2009), high-purity silica glass plates where implanted at 0° of incidence at room temperature with 2 MeV Ag^{2+} (or Au^{2+}) ions at a fluence of 3.35×10^{16} ion/cm^2 (3.10×10^{16} ion/cm^2). The depth of the Ag NPs layer was 0.94 μm with a FWHM of 0.72 μm, while for Au the depth was 0.57 μm with a FWHM of 0.36 μm. After Ag implantation, the samples were thermally annealed for 1 hr in a reducing atmosphere 50%H_2+50%N_2 at a temperature of 600°C for Ag. In the case of Au, an oxidizing atmosphere (air) was used for 1 hr at 1100°C. The metal implanted distributions and fluences were determined by Rutherford Backscattering Spectrometry (RBS) measurements using a 3 MeV $^4He^+$ beam for Ag and a 2 MeV $^4He^+$ beam for Au. Ion implantation and RBS analysis were performed using the IFUNAM's 3MV Tandem accelerator NEC 9SDH-2 Pelletron facility.

Linear optical absorption measurements were performed with an Ocean Optics Dual Channel SD2000 UV-visible spectrophotometer at normal incidence on the surface sample, changing only the incident polarization. The third-order nonlinear optical spectroscopy was performed by the Z-scan method (Sheik-Bahae et al., 1990) at 355, 500, 532, 600 and 750 nm. A picosecond pulsed laser system (PL2143A, 26ps) and an optical parametric generator (PG 401/SH), both from EKSPLA, were used as light sources. These sources were focused with a focal length of 500 mm, where in each case the beam waist was measured by means of the knife's edge method (Khosrofian & Garetz, 1983). The Rayleigh length was calculated to be around 1 cm for all the wavelengths considered, much larger than the thickness of the samples. It was verified that the nonlinear optical response from the SiO_2 matrix was negligible when compared to that from the nanocomposite (matrix + NPs layer). The reference and transmitted beams (open- and closed-aperture) were measured with Thorlabs DET210 fast photodiodes. All optical measurements were performed in the Nonlinear Optics Laboratory at IFUNAM.

3.2 Main results

The linear absorption spectra of the isotropic nanocomposites are shown in Fig. 1. The invariance of the optical absorption for different incident polarizations confirms the optical isotropic behavior. In these Fig., it is also shown the wavelength position of the laser beam used for performing the Z-scan measurements in each case.

Since the plasmonic systems usually exhibit positive and negative nonlinear absorption (NLA) at the same time, a fact that clearly influences the closed-aperture Z-scan traces for nonlinear refraction (NLR), we determined the nonlinear optical coefficients by a theoretical fitting, instead of using the approximate relationships that appear in reference (Sheik-Bahae et al., 1990), as it is usually done. For NLA, the fitting was made following (Liu et al., 2001;

Wang et al., 2010), where the presence of saturable and induced absorption is modeled through the following relationship:

$$\frac{dI}{dz'} = -\left[\frac{\alpha_0}{(1+I/I_0)} + \beta I\right] I, \tag{1}$$

where α_0 is the linear absorption coefficient at the proper wavelength, β is the two-photon absorption coefficient, I is the intensity of the laser, and I_s is the saturation intensity for the saturation of absorption process, respectively. Normally, in the case of third order nonlinear optical phenomena, the NLR contribution is written as $n=n_0+n_2I$, and the NLA as $a=a_0+\beta I$, where n_0 and a_0 are the linear refraction and absorption, respectively; n_2 is the nonlinear refractive index and β is the two-photon absorption coefficient. But when we have saturation of absorption, the first part of Eq. 1 can be developed in series in order to obtain $a \approx a_0 (1-I/I_s)$, where we define a negative NLA coefficient as $\beta=-a_0/I_s$. Then, we can note that, for a proper irradiance, the NLA superposition can result in cancellation of any nonlinear absorption effects. In order to show the nonlinear optical response through the entire spectral range studied, we resume the results in Figs. 2 and 3, where we have included the linear absorption spectra in the graphics in order to see in which zone we were exciting, near or far of the plasmon resonance. It is worth mentioning that we have shown in Fig. 3, the negative and positive values of β obtained when fitting, by using Eq. 1, the experimental data obtained from the z-scan measurements. This will help us later when we discuss the physical origin of the observed nonlinear optical behavior for both plasmonic nanocomposites.

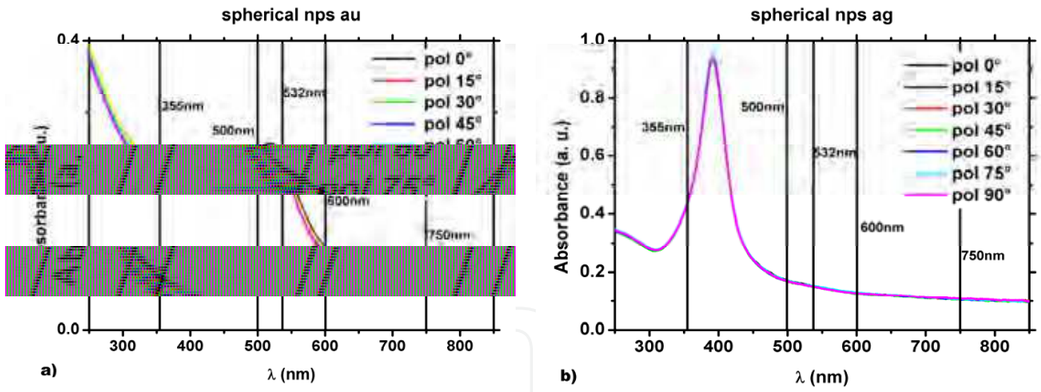

Fig. 1. Linear optical absorption of isotropic samples. a) Au NPs. b) Ag NPs.

In Fig. 2, for the Au nanocomposite, we can see that the NLR is always positive and grows with wavelength, except at the shortest wavelength used (355 nm), where the sign changes. In the case of Ag, the NLR is also positive, but there is a change of sign at 500 nm, near the low-energy side of the plasmon resonance. This change of sign was also found at 532 nm for low irradiances, but it became positive when increasing the irradiance. Then, we argue that, for a higher irradiance at 500 nm, the sign may become positive. This has to do with the type of electronic transition being excited in each case, as it will be discussed later. For NLA (figure 3), a superposition of effects for both types of nanocomposite is clearly seen, confirming that, with the proper irradiance, the nonlinear absorption can be cancelled, as

shown for Ag at 600 nm and for Au at 355 nm. It can be also deduced that, for low irradiances, a positive NLA dominates, whereas at higher irradiances, NLA changes sign, *i.e.*, the nanocomposite's absorption saturates and becomes more transparent.

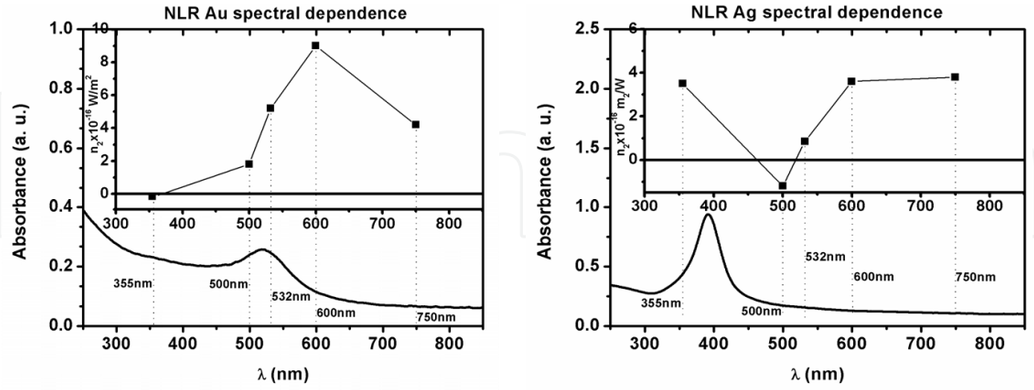

Fig. 2. NLR spectroscopy results for isotropic samples. The upper data of each part show the value of n_2 obtained from the measurements for Au and Ag NPs isotropic samples, while the lower curve is the corresponding linear optical absorption. The dotted vertical lines represent the wavelength where the NLR measurements were performed.

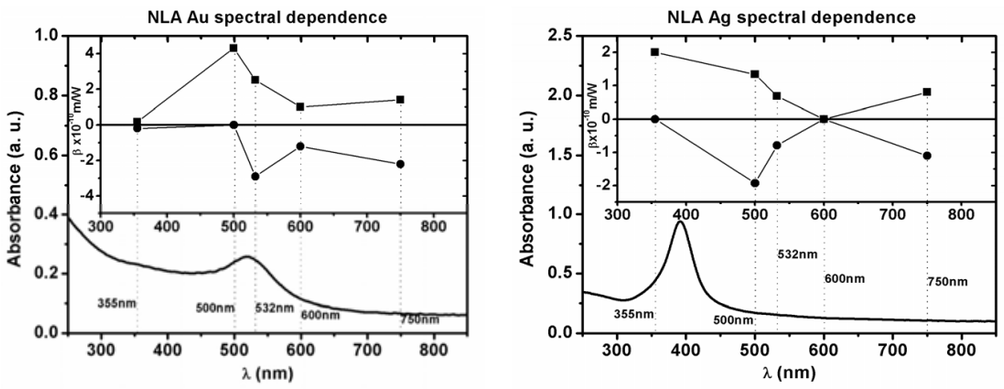

Fig. 3. NLA spectroscopy results for isotropic samples. The upper data of each part show the value of β obtained from the measurements for Au and Ag NPs isotropic samples, while the lower curve is the corresponding linear optical absorption. The dotted vertical lines represent the wavelength where the NLA measurements were performed.

3.3 Discussion

It is well known that the optical response of metallic nanocomposites depends on the excitation wavelength, since the induced effects in the NPs can excite inter- and/or intra-band electronic transitions. In the linear regime, it has been well established that plasmon resonances are due to intra-band transitions, and that they can be explained using Drude's model for metals, by adding a correction of the inter-band transitions when calculating the dielectric function of the NPs (Noguez, 2007). Regarding the nonlinear regime, in the isotropic case, both electronic transitions contribute with the same sign to the nonlinear optical response near the plasmon resonance, as explained by Hache *et al.* (Hache et al.,

1986, 1988). Nevertheless, intra-band transitions are present in the whole visible spectrum, while inter-band only when the respective band-gap is overcame. In the case of gold, this band gap corresponds to 1.7 eV (729 nm) (Hache et al., 1988).

Additionally, there is another contribution to the optical properties in the nonlinear regime. This is the formation of hot-electrons, which contribute with opposite sign to the optical response. Following Hache *et al.* (Hache et al., 1988), near the plasmon resonance, the nonlinear optical response is due, principally, to inter-band transitions and the formation of hot-electrons. Then, both contributions were present when we use 532 nm for Au and 355 nm for Ag, since these wavelengths lay near of the respective plasmon resonances. At low irradiances dominates the inter-band contribution, which is reflected in a positive NLA, but when the irradiance is increased, the formation of hot-electrons increases at the same rate, dominating the optical response and changing the sign of the NLA.

For longer wavelengths, the nonlinear optical response is very similar for both nanocomposites, due to the absence of inter-band transitions. In that region, only the free-electron response, explained by the Drude model, contributes to the optical response, *i.e.*, the intra-band transitions and the hot-electrons. But, because of the low energy of the photons in this region, the hot-electron contribution is not as strong as near the plasmon resonance and, consequently, a positive NLA is always dominant. However, we must consider that the shorter the wavelength, the higher the energy of the photon, consequently, the production of hot-electrons is higher for shorter wavelengths, and the positive NLA ceases to be dominant for a given irradiance and different wavelengths (Fernández-Hernández et al., 2011). For NLR, there is a simple calculation of the NLR index following Boyd (Boyd, 2008), which is given by

$$n_2 = \frac{-e\alpha_0\tau_r}{2\varepsilon_0 n_0 m\hbar\omega^3}, \tag{2}$$

where e is the charge of the electron and τ_r is the response time of the material (300 fs). Introducing the respective values for our nanocomposites, this shows that n_2 is around 10^{-16} m^2/W, of the order of magnitude found in the measurements, as shown in Fig. 2. The entire nonlinear optical response discussed here is due completely to the presence of the NPs into the matrix, because, as it was said before, the nonlinear optical response of the matrix was negligible.

4. Third-order nonlinear optical response from anisotropic metallic nanocomposites

The anisotropy of the metallic nanocomposites makes their nonlinear optical response more complex. Now the dependence on the angular position of the sample and on the incident polarization, due to the form of the third-order nonlinear susceptibility tensor, may cause that the contributions to this response come not only from the inter-band transitions, but also from the intra-band transitions and the hot-electron contribution from two surface plasmon resonances, the one associated to the minor axis and the one associated to the major one.

4.1 Synthesis of anisotropic metallic nanocomposites and optical measurements

For the anisotropic nanocomposites, the previously implanted silica plates were cut into several pieces and each piece was irradiated at room temperature with 8 MeV Si ions at a

fluence of 5.0×10^{15} ions/cm^2 for Ag, and 10 MeV Si ions at a fluence of 1.2×10^{16} ions/cm^2 for Au. The Si irradiation was performed under an angle off normal of θ = (0.0° or 80.0°± 0.5°) for both, Ag and Au. As it has shown before in previous works (Oliver et al., 2006; Rodríguez-Iglesias et al., 2008), this irradiation deforms the formed NPs, transforming them in prolate spheroids all oriented along the direction of irradiation. The Si irradiation was also performed using the IFUNAM's 3MV Tandem accelerator NEC 9SDH-2 Pelletron facility. Regarding the nonlinear optical measurements, they were performed for different incident polarizations, 0°, 45° and 90° for normal incidence of light, where 0° corresponds to the polarization aligned with major axis of the NP, and 90° to polarization aligned with the NP minor axis, for deformation at 80°. This convention was also maintained for nanocomposites deformed at 0°.

4.2 Results

The linear absorption spectra of the anisotropic nanocomposites, where the NPs were deformed at 0° and 80°, respectively, are shown in Figs. 4 and 5. The spectra for different polarizations show isotropy for deformation at 0°, as it was expected, because the light's

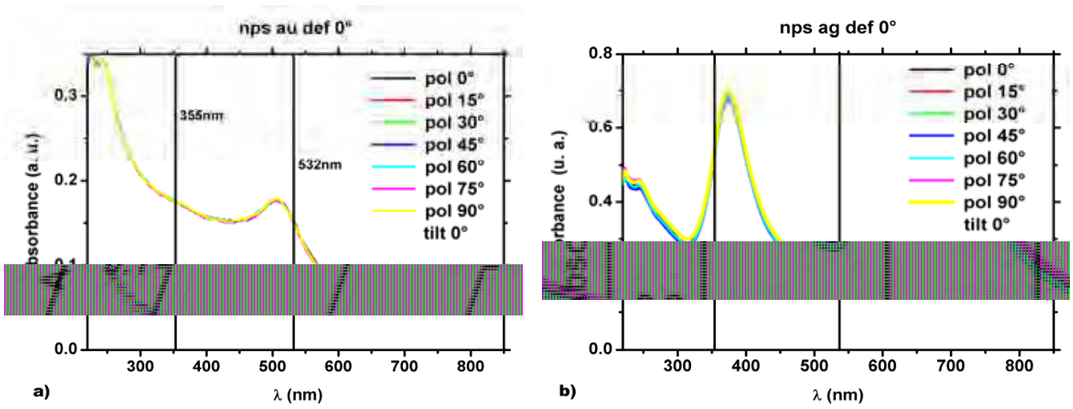

Fig. 4. Linear optical absorption of anisotropic samples with NPs deformed at 0°.
a) Au NPs. b) Ag NPs.

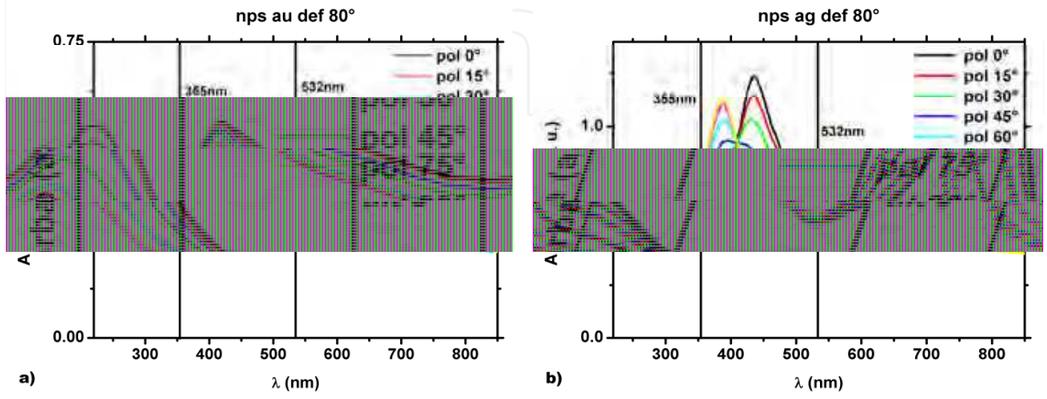

Fig. 5. Linear optical absorption of anisotropic samples with NPs deformed at 80°.
a) Au NPs. b) Ag NPs.

polarization is parallel in all cases to the minor axis of the deformed NPs; while the anisotropic optical behavior is clear for deformation at 80° when varying the polarization. This last behavior can be explained with the presence of a second plasmon resonance at higher wavelengths, which corresponds to the major axis of the NPs. As before, in these Figs., it is also shown the wavelength position of the laser beam used for performing the Z-scan measurements in each case.

Regarding the nonlinear response of the anisotropic plasmonic nanocomposites, Figs. 6-9 show the results for both type of nanocomposites, deformed at 0° and 80°, where we have used only the wavelengths of 532 nm and 355 nm, as indicated previously in Figs. 4-5. As said before, the incident polarization angles used were 0°, 45° and 90° for normal incidence of light, with 0° corresponding to polarization aligned with major axis of the NP, and 90° to polarization aligned with the NP minor axis, for deformation at 80°.

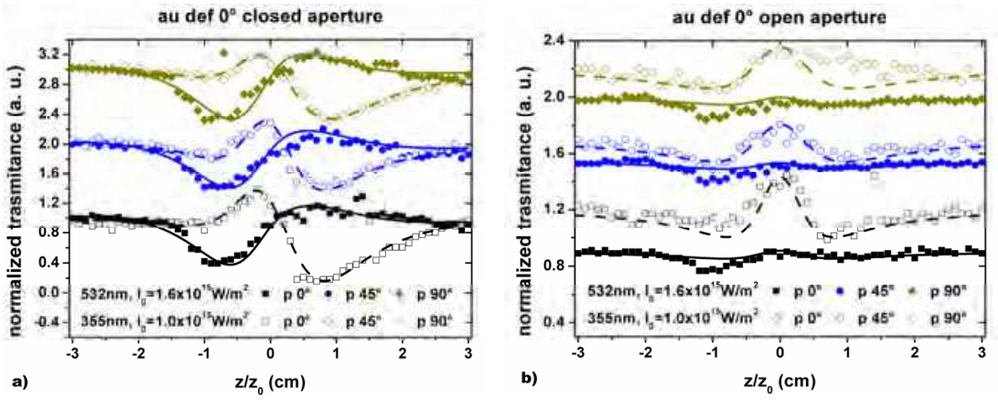

Fig. 6. a) Closed- and b) open-aperture Z-scan for the anisotropic nanocomposite with Au NPs deformed at 0°. Different symbols are used for the different incident polarizations. The empty symbols are used for data obtained at 355 nm, while the filled ones are used for data obtained at 532 nm. Lines represent the fitting to these data. The data sets for different polarizations have been vertically shifted for clarity.

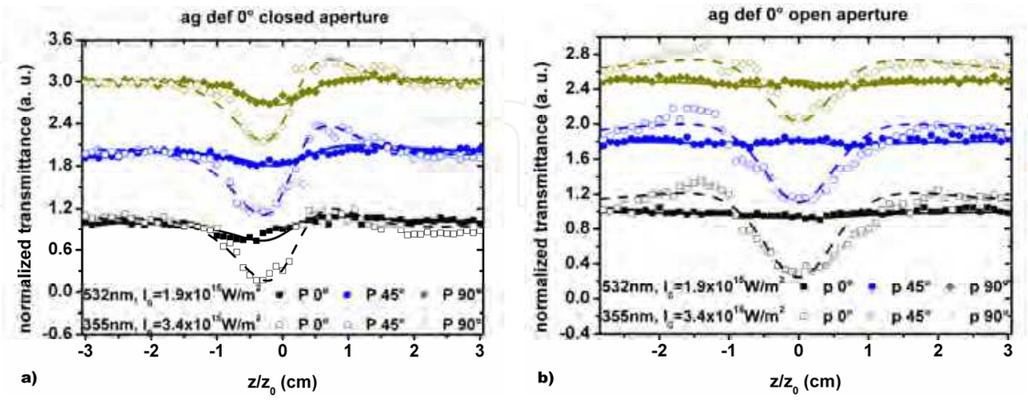

Fig. 7. a) Closed- and b) open-aperture Z-scan for the anisotropic nanocomposite with Ag NPs deformed at 0°. Different symbols are used for the different incident polarizations. The empty symbols are used for data obtained at 355 nm, while the filled ones are used for data obtained at 532 nm. Lines represent the fitting to these data. The data sets for different polarizations have been vertically shifted for clarity.

Figures 6-7 show the nonlinear spectroscopy in the case of deformation at 0°, for both Au and Ag. It is remarkable the independence of the measurements on the incident polarization, confirming the isotropy of the deformed NPs into its transversal section. In the case of Au, there is a clear change of sign in NLR when passing from 532 nm to 355 nm, as in the isotropic case, where the former wavelength lays on the plasmon resonance and the last into the inter-band electronic transitions region. In the case of NLA, a superposition of both saturable and induced absorption is clearly observed for both wavelengths; but at 532 nm, for comparable irradiances, these effects almost cancel each other in both nanocomposites.

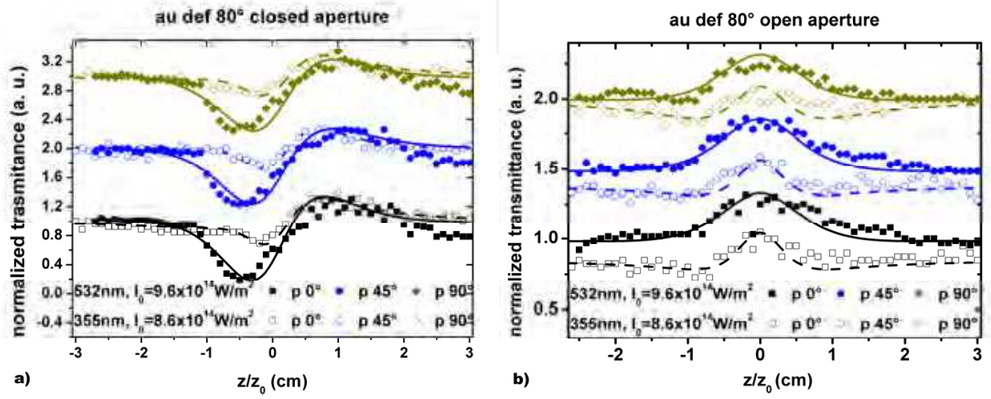

Fig. 8. a) Closed- and b) open-aperture Z-scan for anisotropic nanocomposite with Au NPs deformed at 80°. Different symbols are used for the different incident polarizations. The empty symbols are used for data obtained at 355 nm, while the filled ones are used for data obtained at 532 nm. Lines represent the fitting to these data.

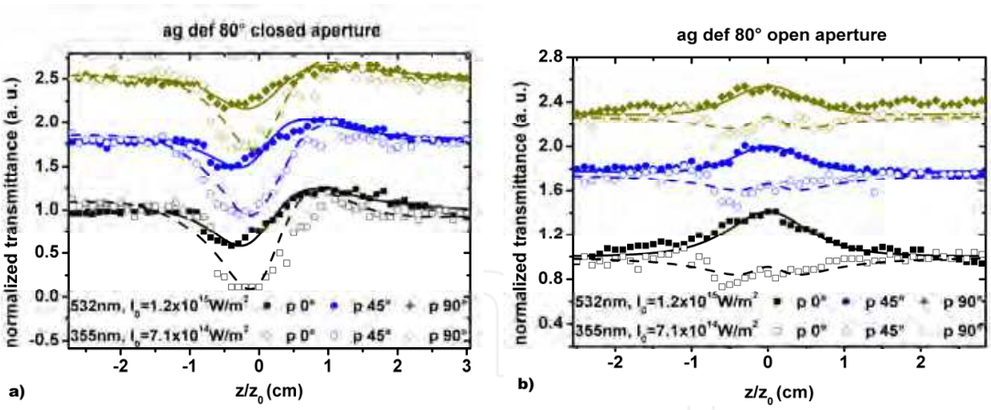

Fig. 9. a) Closed- and b) open-aperture Z-scan for anisotropic nanocomposite with Ag NPs deformed at 80°. Different symbols are used for the different incident polarizations. The empty symbols are used for data obtained at 355 nm, while the filled ones are used for data obtained at 532 nm. Lines represent the fitting to these data.

In the case of NPs deformed at 80°, from Figs. 8 and 9, it can be seen that, for NLR, in both nanocomposites, there is not a change of sign, but the magnitude of the response is larger when exciting near the plasmon resonances, 532 nm in the case of Au nanocomposite, and 355 nm in the case of Ag one. For NLA, a superposition of effects with different sign is present again in both samples, where saturable absorption dominates at 532 nm.

4.3 Analysis

Regarding the anisotropic nanocomposites, as reported recently (Reyes-Esqueda et al., 2009; Rodríguez-Iglesias et al., 2009), there are three linearly independent components of the third order nonlinear susceptibility tensor that are responsible for the optical response of the nanocomposite, one of them corresponding to the mayor axis of the NP, another to the minor axis, and a final one to a linear superposition of them. Consequently, the third-order nonlinear polarization for the anisotropic nanocomposite may be written in terms of the angle between the electric field and the NP's axis, which defines the optical axis of the nanocomposite, as

$$\mathbf{P}_{\mathbf{NL}}^{(3)}(\theta;\omega) = 3\left|E(\omega)\right|^2 E(\omega)\left[\chi_{1111}^{(3)}\sin^3\theta\hat{\mathbf{j}} + \frac{3}{2}\chi_{1133}^{(3)}\sin 2\theta\left\{\cos\theta\hat{\mathbf{j}} + \sin\theta\hat{\mathbf{k}}\right\} + \chi_{3333}^{(3)}\cos^3\theta\hat{\mathbf{k}}\right]. \quad (3)$$

When the incident electric field is parallel to the minor axis, the nonlinear polarization is trivially given by

$$\mathbf{P}_{\mathbf{NL}}^{(3)}(\theta;\omega) = 3\left|E(\omega)\right|^2 E(\omega)\chi_{1111}^{(3)}\hat{\mathbf{i}}. \quad (4)$$

These two equation allows us to analyze the results presented in Figs. 6-9. For the case of deformation at 0°, the incident electric field is clearly parallel to the minor axis of the NP, being then Eq. 4 the correct one. According to our previous results (Silva-Pereyra et al., 2010), the minor axis of the NP has a size very similar to the radius of the isotropic NPs. Then, in this case, independently of the polarization, the incident light sees always an isotropic metallic system. Therefore, one can explain the results presented at Figs. 6 and 7 in a similar way as explained for the isotropic case. For Au, at 355 nm, the inter-band transitions contribute the most to the nonlinear optical response. At 532 nm, the intra-band transitions and the hot-electron contribution dominate now the optical response. For Ag, at 355 nm, the intra-band transitions and the hot-electron contribution dominate now; but, for 532 nm, there is only the intra-band transition contributing to the optical response. For both cases, one can see the same behavior as for the isotropic case.

But for deformation at 80°, this analysis is more difficult. Now, for incident polarization of 0°, Eq. 3 is the correct one to try to explain the nonlinear optical response observed. In this case, since the measurements are performed at normal incidence, the angle between the electric field and the major axis of the NP is 10°. By evaluating this into Eq. 3, one can observe that the larger contribution to the observed behavior comes from the term corresponding to the major axis, that is, $\chi_{3333}^{(3)}$, although there is also a contribution from the term mixing the axes, $\chi_{1133}^{(3)}$, and then the contribution from the plasmon resonances. Fortunately, for the wavelengths used in this work, the analysis may be done considering only one plasmon resonance at a time. This fact allows making the same considerations as for the isotropic case, and, for applications, by varying wavelength, polarization and angular position of the sample, one can switch the sign of the nonlinear optical response of these nanocomposites. For example, for Ag at 355 nm, the resonance associated to the major axis almost does not contribute to the optical response since it is rather far from this wavelength. Similarly, the inter-band transitions do not contribute. Then, the observed response is mostly due to the intra-band transitions and the hot-electron contributions from

the resonance associated to the minor axis. But this is exactly what happened for the isotropic case and for the NPs deformed at 0°. In the case of Au at 532 nm, the inter-band transitions do not contribute, but now, both resonances contribute to the observed response, although the wavelength is nearest to the resonance associated to the major axis, which presents also a larger absorbance, increasing the magnitude of the nonlinearity measured too. For incident polarization of 90°, Eq. 4 again describes the observed response, which is again, in general, as for the isotropic case. However, for the deformation at 80°, for Au, there is one discrepancy at 355 nm, for both polarizations the NLR turns to be positive, while for deformation at 0° and for the isotropic case, this was negative. This result deserves a more careful analysis, which will be done at some other time.

5. Second-order nonlinear optical response for anisotropic nanocomposites

Although anisotropic metallic NPs are still centrosymmetrical systems, there is the possibility of measuring SHG from them when higher order interactions, like electric quadrupole, and magnetic dipole responses from the NPs bulk, and/or electric dipole responses allowed from the NPs surfaces (Aktsipetrov et al., 1995; Brevet et al., 2011; Dadap et al., 1999, 2004; Figliozze et al., 2005; Gallet et al., 2003; Mendoza et al., 2006), where the inversion symmetry of the bulk material is broken, are present. The latter response dominates in the specific case the NP size is much smaller than the wavelength of the exciting (fundamental) beam (Aktsipetrov et al., 1995), so that field retardation effects (no spatial dependence of the electromagnetic fields) are neglected.

5.1 Theoretical analysis

In general, the second-order nonlinear polarization, $P_i^{(2)}$, induced by an incident electric field, *E*, for the bulk second-order susceptibility, $\chi_{ijk}^{(2)}$, is given by $P_i^{(2)} = \chi_{ijk}^{(2)} E_j E_k$. For materials composed of nonlinear optical scatterers much smaller than the wavelength of the fundamental beam, such as in the case of thin films composed of syntectic macromolecules or fibrillar proteins for instance (Knoesen et al., 2004; Leray et al., 2004; Podlipensky et al., 2003; Rocha-Mendoza et al., 2007), the origins of the bulk second-order susceptibility $\chi_{ijk}^{(2)}$ comes from the coherent summation of the molecular hyperpolarizability $\beta_{i'j'k'}$ of the smaller molecules. In a similar way, due to the fact that the elongated NPs of our samples are at least a hundred times smaller than the wavelength of the fundamental light and in the limit of weak coupling between each nonlinear NP, we can express the macroscopic susceptibility of the thick layer containing NPs as

$$\chi_{ijk}^{(2)} = N \sum \left\langle R_{ijk,i'j'k'} \right\rangle \beta_{i'j'k'} . \tag{5}$$

where *N* is the number density of NPs contained within the point spread function of the beam, $\beta_{i'j'k'}$ is the hyperpolarizability tensor for the NPs, and $R_{ijk,i'j'k'}$ are the elements of the Euler rotation matrix that transforms the hyperpolarizability $\beta_{i'j'k'}$ in the NPs coordinate system ($i'j'k' = \xi, \eta, \zeta$) to the laboratory coordinates ($ijk = x, y, z$). The angular averaging denoted by $\langle\ \rangle$ accounts for the angular distribution of the NPs. Fig. 10 shows a

schematic representation of the Euler angles, where the z-axis is normal to the sample surface and the ζ-axis is along the NP long axis. Assuming the interface between the glass substrate and the NPs layer to be azimuthally isotropic (invariance under ψ-rotation), i. e. this interface does not contribute to the second harmonic signal, there are only three nonvanishing independent components of $\chi^{(2)}$, $\chi^{(2)}_{xxz} = \chi^{(2)}_{yyz} = \chi^{(2)}_{xzx} = \chi^{(2)}_{yzy}$, $\chi^{(2)}_{zxx} = \chi^{(2)}_{zyy}$ and $\chi^{(2)}_{zzz}$.

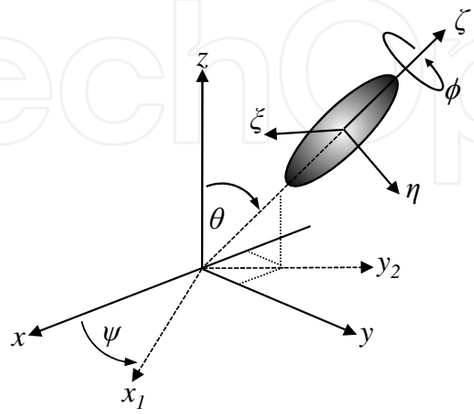

Fig. 10. Euler angles, (ψ,θ,ϕ), relating the laboratory coordinates system, xyz, and the coordinate system, $\xi\eta\zeta$, of a single El Ag-NP. ϕ is the isotropic azimuthal angle over the ζ-axis. $x1$-axis is obtained from the first rotation, ϕ. θ is the pitch angle formed from the z-axis of the laboratory system and the ζ−axis of the NP coordinate system, after the first rotation ϕ. ψ is the azimuthal angle over z-axis.

It is common practice to calculate the average orientation of the sub-molecular units that give rise to the macroscopic susceptibility of nonlinear materials using SHG/SFG experiments. In the process, analytical expressions of the independent tensor components are typically written in terms of the pitch angle, θ, defined by the z-axis and the noncentrosymmetric subunit ζ-axis, and the resulting nonzero elements of the microscopic hyperpolarizability, $\beta_{i'j'k'}$. Such expressions and their derivation are found elsewhere [16-19,24], and will not be rewritten here. Instead, for the purpose of this work, we followed the formalism used in Refs. (Hirose et al., 1992; Knoesen et al., 2004; Zhuang et al., 1999) to derive expressions for the effective susceptibility tensor, $\chi^{(2)}_{eff}$, in terms of the experimental variables α and ϕ. With α as the angle of the linearly polarized fundamental beam with respect to the plane of incidence, and, ϕ, as the angle made by the projection of the NP long axis, ζ, over the xy plane and the fixed plane of incidence contained in xz. From Fig. 10 we can deduce that $\phi = \psi + 90°$. The total SH intensity is proportional to the sum of the effective susceptibility p and s as follows

$$I_{SH} \propto \left|\chi^{(2)}_{eff}\right|^2 = \left|\chi^{(2)}_{eff,p\alpha}\right|^2 + \left|\chi^{(2)}_{eff,s\alpha}\right|^2, \tag{6}$$

where the first and second sub indexes (from left to right) of $\chi^{(2)}_{eff}$ in the right-hand side of Eqn. 6 denote the output (fixed) and input (variable) polarization directions, respectively, and each component can be computed from

$$\chi^{(2)}_{eff,\hat{e}_2\hat{e}_1} = \left[\hat{e}_2(2\omega)\cdot\vec{L}(2\omega)\right]\cdot\chi^{(2)}:\left[\hat{e}_1(\omega)\cdot\vec{L}(\omega)\right]^2, \tag{7}$$

Here $\hat{e}_1$ and $\hat{e}_2$ are the unit polarization vectors of the fundamental and SHG beams, respectively. With $\hat{e}_1$ (or α) =0º (or 180º) for *p*-polarized light and 90º (or 270º) for *s*-polarized light, for example. $\vec{L}(\Omega)$ is the Fresnel factor at frequency Ω at the silicon substrate and nonlinear media interface. This parameter is found to be quite sensitive in the determination of molecular orientation since it depends on the index of refraction of the interfaces involved and the cosine of the angle of incidence/reflection of the fundamental/SH beam (Zhuang et al., 1999). However, we already know the orientation angle of the NPs and for simplicity, we will approximate this values to unity.

In the first approximation, we chose to model the elongated NPs as rod particles for which the hyperpolarizability tensor is cylindrically symmetric along ζ (invariance under ϕ-rotation). We also assume that the optical frequencies of the fundamental and SH beams are not in resonance with electronic transitions, so that there are only two nonvanishing independent components ($\beta_{\xi\xi\zeta} = \beta_{\eta\eta\zeta}$, and $\beta_{\zeta\zeta\zeta}$). Under these conditions using Eqs. 5 and 7 we obtain

$$\begin{aligned}
\chi^{(2)}_{eff,p\alpha} &= \frac{-1}{4}a\sin 2\alpha\sin\phi\left(\cos\phi+\sin^2\phi\right)r \\
&+\frac{\sqrt{2}}{2}a\cos^2\alpha\sin^2\frac{\phi}{2}\left(r\sin^2\phi+\cos^2\phi\right) \\
&-\frac{\sqrt{2}}{2}ab\cos\phi\sin^2\phi\left(1-\frac{1}{2}\cos^2\alpha\right) \\
&+\frac{1}{4}a\sin 2\alpha\sin 2\phi\sin^2\frac{\phi}{2}
\end{aligned} \tag{8}$$

for *p*-SH and

$$\begin{aligned}
\chi^{(2)}_{eff,s\alpha} &= \frac{-\sqrt{2}}{4}a\sin^2\alpha\sin^3\phi \\
&-\frac{\sqrt{2}}{4}\sin\phi\left(1+\cos^2\phi\right)r \\
&-\frac{\sqrt{2}}{4}\sin\phi\cos^2\alpha\left(\cos\phi-\sin^2\phi\right)r \\
&+\frac{1}{2}a\sin 2\alpha\left(\cos^2\phi\sin^2\frac{\phi}{2}r+\sin^2\phi\cos^2\frac{\phi}{2}\right)
\end{aligned} \tag{9}$$

for *s*-SH, respectively.

In Eqs. (8) and (9) $r=\beta_{\xi\xi\xi}/\beta_{\zeta\zeta\zeta}$ and $a=N\beta_{\zeta\zeta\zeta}$ are our fitting parameters, while *b*=1-*r*. Note that $\chi^{(2)}_{eff,p\alpha}=\chi^{(2)}_{eff,s\alpha}=0$, in the specific case when ϕ=0, this result is expected since under this configuration the input electric field finds isotropically shaped NPs. For all other configurations (ϕ=90°; ϕ=180° and ϕ=270) $\chi^{(2)}_{eff,p\alpha}\neq\chi^{(2)}_{eff,s\alpha}\neq 0$ and polar traces with different lobes of maximum SH are found for *p*- and *s*-SH, respectively, as will be shown in our discussions.

5.2 Sample preparation and optical measurements

The anisotropic Ag nanocomposites used for SHG measurements were prepared as before, only the angle of deformation was modified to 45° and the fluences were 2.4×10^{17} ion/cm^2 for Ag, and 1×10^{16} ion/cm^2 for Si. The depth of the layer of elongated NPs was 0.9 μm with a FWHM of 0.5 μm.

In order to characterize the NPs orientation in the samples, prior to the SHG experiments, we collected optical absorption spectra using linearly polarized light at two mutually orthogonal polarizations, one parallel (labeled as *p*) and the other perpendicular (labeled as *s*) to the plane of incidence. This experiment was performed at three different angles of incidence (0^o and $\pm45^o$) and an UV-visible spectrophotometer was used to perform the measurements. Figure 11 shows the schematic of these experiments (a and b) and the respective absorption spectra (d and e). Note that Fig. 11 a and b resembles the resulting samples of the two ion implantation process. Note that in Fig. 11 b the particles long axes are tilted 45^o with respect to the substrate normal and lay on the *xz* planes of the laboratory *xyz* coordinate system. When viewed from the front, the projection of the long axes of the deformed NPs point in the direction we label as *x*.

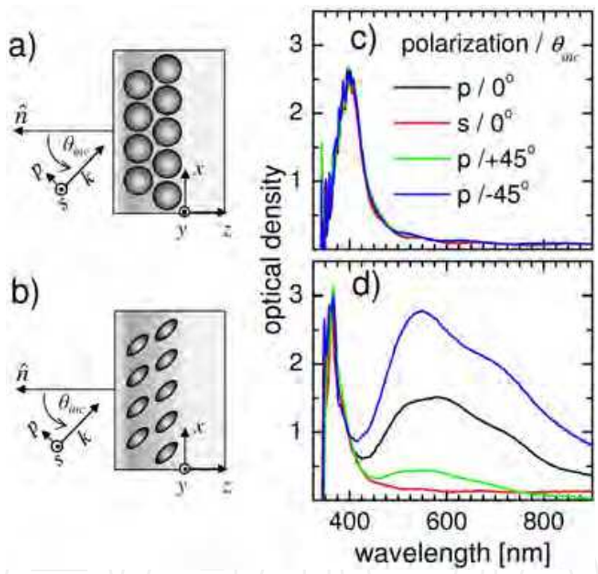

Fig. 11. Schematics for absorption experiments on spherical (a) and elongated (b) Ag-NPs. In the figures, *xyz* is the laboratory coordinate system; *p* and *s* are respectively the parallel and perpendicular linear polarization of the incident beam with respect the plane of incidence; θ_{inc} is the angle of incidence (positive for counterclockwise direction) made by the propagation direction, *k*, and the surface normal, $\hat{n}$. (c) and (d) are the absorption spectra of spherical and elongated Ag NPs respectively, taken at different input polarization and angle of incidence (as labeled in (c)).

The absorption spectra taken under different angles of incidence have no significant changes for the case of spherical NPs samples. This is shown in Fig. 11c, where a single SP resonance is found at approximately 400 nm. In contrast, from Fig. 11d we can see that for the elongated NPs the absorption spectra depends on both the light polarization and the angle

of incidence. At normal incidence the SP resonance of the particles is shifted to lower wavelengths for *s*-polarization (red line), while the absorption spectra splits into two spectrally separated SP resonances for *p*-polarization (black line). The shifted resonance at 365 nm obtained with *s*-polarized light is associated with the short-axis SP and can be explained by the decrease of the NPs size (McMahon et al., 2007) during the second ion implantation process. The resonance at 570 nm obtained with *p*-polarized light is associated with the long-axis SP and its broadness can be explained by the different NPs sizes formed in the matrix. Note that the 365 nm resonance is also present and presumably invariant in the spectra taken at the three angles of incidence with *p*-polarized beams, i. e. at -45^o (blue line), 0^o (black line) and 45^o (green line). While in the case of *p*-polarized light at 45^o this result is obvious, since it resembles the case of *s*-polarized light at 0^o, the presence of this band in the other two cases, 0^o and -45^o, can be attributed to a residual misalignment with respect to the direction of elongation of the particles, or to an actual fraction of smaller spherical NPs remaining in the matrix after the second ion-implantation process. Finally, a strong dependence of the 570 nm SP is obtained with *p*-polarized light for different angles of incidence being higher when the light propagation is orthogonal to the NPs axes (blue curve). This last result was the criteria used to characterize the NPs orientation used in the SHG experiments.

SHG experiments in the reflection mode with a fixed angle of incidence were conducted using a Ti:Sapphire oscillator as the fundamental beam. The schematic representation of these experiments is shown in Fig. 12a. The laser delivered linearly polarized femto-second pulses with a wavelength centered at 825 nm (pulse width, 88 fs; repetition rate, 94 MHz). The angle of polarization, α, of the fundamental beam was rotated using a $\lambda/2$ wave-plate in order to trace the polar SH dependence of our samples. Using a 50 mm focal length lens, the

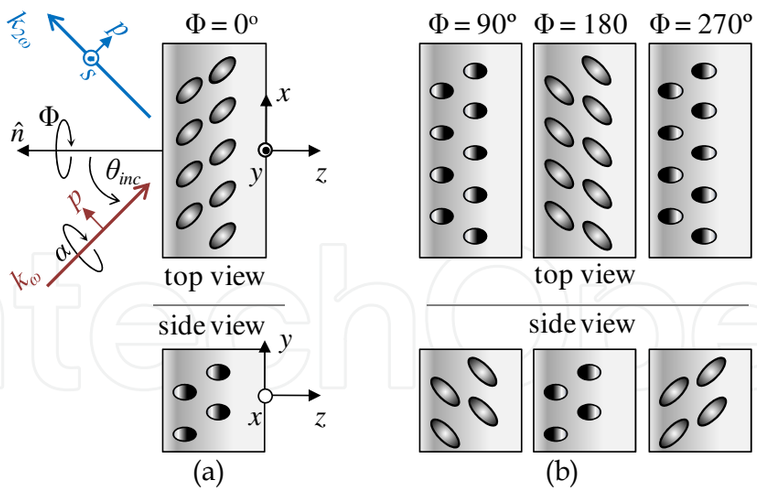

Fig. 12. a) SHG experiment in the reflection mode. In the figure, ω,2ω: fundamental and the second harmonic frequencies; *p*/*s*:parallel/perpendicular linear polarization of the incident beam with respect the plane of incidence; θ_{inc} : angle of incidence made by the propagation direction, $k\omega$, and the surface normal, $\hat{n}$; α : angle of polarization of the fundamental beam; ϕ: sample rotation angle made by the projection of the NP long axis, ζ, over the *xy* plane and the fixed plane of incidence contained in *xz*. (b) Different sample orientations, i. e., elongated NPs orientations with respect the laboratory system, used on SHG experiments.

beam was focused onto the nanocomposite at an angle of incidence $\theta_{inc} = 45°$ with respect the sample surface normal. The reflected SH signal was collected at 90^o with respect to the incoming light using a second lens of 30 mm focal length. A color filter and a grating monochromator (not shown) were used to spectrally separate the SH signal from the fundamental light. Finally, the signal was detected via a photomultiplier tube connected to a current/voltage pre-amplifier circuit and a digital oscilloscope. The *p*-polarized SH (*p*-SH) and *s*-polarized SH (*s*-SH) intensities were also measured using a polarizer cube before signal collection. The sample was mounted on a rotation stage in order to vary the NPs long axis orientation by rotating the angle ϕ. The four different angles used in our experiments are represented in Fig. 12b.

5.3 Results and discussion

Figure 13 shows both the measured and simulated polar dependence of the total (black), *p*-polarized (red) and *s*-polarized (blue), SHG intensities obtained for the different 90^o-shifted ϕ configurations described in Sec. 5.2. Note that in the experiment, the four configurations produced detectable *p*- and/or *s*-SHG signal. We stress out that, in principle, even when the centrosymmetry of the ellipsoidal and spherical NPs is locally disrupted by its surface, the homogeneous polarizing field induces SHG of mutually cancelling polarizations at opposite sides of the circular surface, neglecting then an overall dipolar SHG contribution (Figliozzi et al., 2005; Mendoza & Mochan, 2006). However, we have to bear in mind that no perfect ellipsoids (or spheres) are present in our samples and that the NP size is almost two orders of magnitude smaller that the excitation beam to consider the SH signal as a quadripolar contribution from the NPs bulk. In addition, according to rigorous calculations made by Valencia *et. al.* (Valencia et al., 2004, 2009), SHG radiation from centrosymmetric infinite cylinders is not symmetric in the back and front surfaces. They find a multi-lobe SHG pattern originated at the cylinder surface, where the angle made from the first SHG scattered lobes in the first surface is more pronounced as the cylinder width is decreased. Seemingly, Bachelier *et. al.* (Bachelier et al., 2010) modeled both the near-field of the harmonic amplitude and the far-field SH intensity distribution in spherical gold NPs, the two cases show anisotropic radiation patterns arising from the NP surface. Therefore, we attribute this signal to a nonlinear dipolar contribution arising from the NPs surface.

Figure 13a shows, for example, the case when the incident beam is polarized perpendicular to the NP long axis (see Fig. 12a; $\phi = 0^o$). Here the cross section of the elongated NPs could be considered circularly shaped (from the incident fundamental beam point of view) and therefore no SHG signal is expected according to Eqs. 8-9. In this case, in addition to our argument that no perfect circularly shaped NPs cross section are present in the sample, we attribute this signal to a systematic misalignment in the experiment while rotating the samples as will be shown latter. In contrast, lobes of maximum SH intensity are found at α-angles near the NPs long axes. This is seen in Figs. 13b and d ($\phi = 90^o$ and $\phi = 270^o$), respectively, where the *s*-SH intensity is the main contribution of the total SH signal. Seemingly, the main contribution in Fig. 13c ($\phi = 180^o$) is the *p*-SH, instead. Note that Figs. 12b and d are basically mirror images of each other (with *y*, or $\alpha = 90^o$, as the symmetry axis) with total SHG maxima at $\sim 115^o$ and $\sim 290^o$, for b, and $\sim 65^o$ and $\sim 255^o$ for d, respectively; the counterpart *p*-SH intensity has practically no contribution. Otherwise, from Fig. 13c we can see that both the *p*- and *s*-SH intensities contribute to the total SH when the fundamental beam is perpendicular to the NPs long axes (Fig. 12b; $\phi = 180^o$).

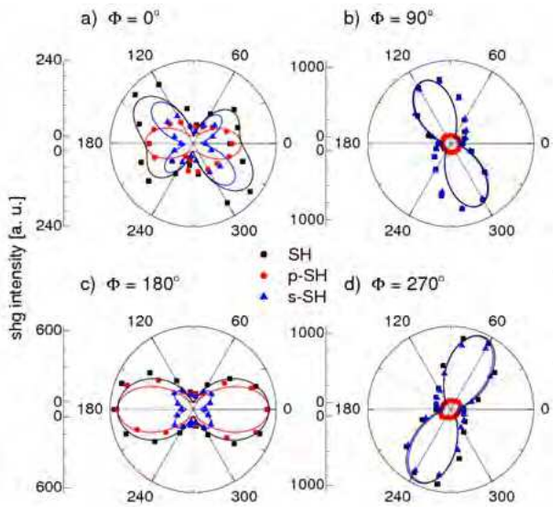

Fig. 13. Experimental and simulated SHG polar dependence of elongated Ag NPs, for the four different sample orientations (see Fig. 4) ϕ=0^o (a), ϕ=90^o (b), ϕ=180^o (c) and ϕ=270^o (d), respectively. In all plots the experimental total, *p*-polarized and *s*-polarized, SH are denoted by black squares, red circles and blue triangles, respectively. While the simulated SHG intensities are denoted using the same color convention in solid lines. An offset has been intentionally added in all plots to see the lower signal (see *p* -SH in b and d, for example).

The simulated polar traces are in a good agreement with the experimental results; this can be seen also in Fig. 13. Table 1 shows specific values of the parameters *r* and *a*, used in Eqs. 8-9, that best fitted with the experimental data, where, ϕ_{sim}, stands for the simulated value of ϕ. The simulated data revealed two extra peaks in between the *s*-SH maxima (~ 25 times lower), in Figs. 13b and d, respectively, and their values are found also in Tab. 1. Seemingly, two extra peaks are also found in Fig. 13c, but at much smaller values (~ 300 times less). Note also that the values of *r* were fitted in the range of $1.4<1/r<3.5$ for cases 2−4 (see table), confirming that there is a stronger hyperpolarizability response for fields oscillating along the NPs long axis (i.e. $\beta_{\zeta\zeta\zeta} > \beta_{\xi\xi\xi}$). These values are very similar to the values obtained in synthetic films consisting of helical (PBLG) macromolecules (Knoesen et al., 2004) and native fibrillar collagen (Stoller et al., 2003), their hyperpolarizability are reported to be within an order of magnitude of that of crystalline quartz (Freund et al., 1986).

Case	ϕ	$1/r$	a	ϕ_{sim}	$\left\|\chi^{(2)}_{eff,p\alpha}\right\|^2_{max}$	$\left\|\chi^{(2)}_{eff,s\alpha}\right\|^2_{max}$
1.	0^o	1/1.41	16	176^o	0^o, 180^o	45^o, 135^o
2.	90^o	3.5	52	87^o	25^o, 115^o 205^o, 295^o	65^o, 155^o 245^o, 335^o
3.	180^o	1.4	34	180^o	0^o, 90^o 180^o, 270^o	45^o, 135^o 225^o, 315^o
4.	270^o	3.5	57	271^o	66^o, 156^o 246^o, 336^o	26^o, 116^o 206^o, 295^o

Table 1. Values of parameters, *r* and *a*, and resulting SH maxima positions, to simulate the SHG experiments on elongated Ag NPs.

Note that simulating the different cases shown in Figs. 13b-c with the same parameters (*r* and *a*) would result in obtaining higher SHG maxima in Fig. 13c than in Figs. 13b and d. However, in the experiment we obtained less SHG signal in Fig. 13d and we attribute this result to the presence of less NPs within the point spread function of the fundamental beam and/or a minor hyperpolarizability value. The inhomogeneous NPs distribution in the composite film makes extremely challenging maintaining the same irradiated area in the experiment while rotating the sample. As a consequence, the value of the parameters *a* and *r* used to fit the experimental data were different. As can be seen from Tab. 1, in this experiment the parameters used in Fig. 13c resulted to be smaller than the respective parameter values used to fit the experimental data of Figs. 13b and d. Otherwise, it is interesting to note that the experimental case at $\phi = 0^o$ (Fig. 13a) is reproduced for angles ϕ_{sim} close to 180^o and $r = 1.41$, this simply indicates that we can simulate this result by assuming stronger hyperpoplarizability responses for fields oscillating perpendicular to the NPs long axis (*i.e.* $\beta_{\zeta\zeta\zeta} < \beta_{\xi\xi\zeta}$). The asymmetric polar dependence was obtained using ϕ_{sim} confirming that our experimental results are most probable due to misalignment. Note also that both the p- and s-SHG intensities are comparable in magnitude, while for the case shown in Fig. 13c the *p*-SH intensity is ~5 times larger than *s*-SH.

In order to be sure that the results correlate indeed with the known (simulated) structure of the elongated NPs, SHG experiments were also made in spherical NPs. Figure 14 shows SH signal from samples with embedded spherical NPs. The total SHG (black) presents nearly isotropic polar trace where *p*-SH (red) is the maximum signal contribution. The *s*-SH intensity (blue) also contributes but the signal is ~10 times lower than the *p*-SH counterpart. It presents a characteristic shape with maxima at 45^o, 135^o, 225^o and 315^o. We found the same dependence for different ϕ values 0^o and 90^o (Fig. 14a and b), respectively, indicating that the obtained polar traces are a characteristic of the spherical NPs. The fundamental and SH beams spectra for elongated (black) and spherical (red) NPs, with the respective absorption spectra (dotted curves) are also shown in Fig. 15a. The absorption traces indicate that for elongated NPs the SHG may be enhanced since the fundamental is close to resonance with the SP broad band (black dotted line) at 570 nm (see also blue curve on Fig. 11d). Note, however, that the SHG suffers also absorption of about the same optical density reducing the signal. In contrast, the SP resonance of spherical NPs (red dotted line in Fig. 15a; which is the red solid line in Fig. 11c) is far away of the fundamental wavelength and therefore no enhancement effect is expected. In addition since the NPs sizes are small compared to the fundamental wavelength, this suggest that the SHG in spherical NPs samples arises mainly from the electric dipole surface contribution, owing to the actual non perfect spherical shape of the particles (Nappa et al., 2005), and must be large enough to be detectable even after being absorbed with an optical density of ~3. Otherwise, the quadratic dependence with respect to the input power obtained in both types of samples, Fig. 15b (for elongated NPs) and c (for spherical ones), indicates the typical coherent nature of nonlinear scatterers. In particular, the result obtained in spherical NPs indicates that the SH observed is not due to grating effects such as the hyper Rayleigh scattering (HRS), where incoherent SHG is produced for which a typical linear dependence with respect to the input power is observed.

Our results are in accordance with earlier SHG experiments performed by Podlipensky *et. al.* (Podlipensky et al., 2003) on elongated Ag NPs. The main differences with respect to our

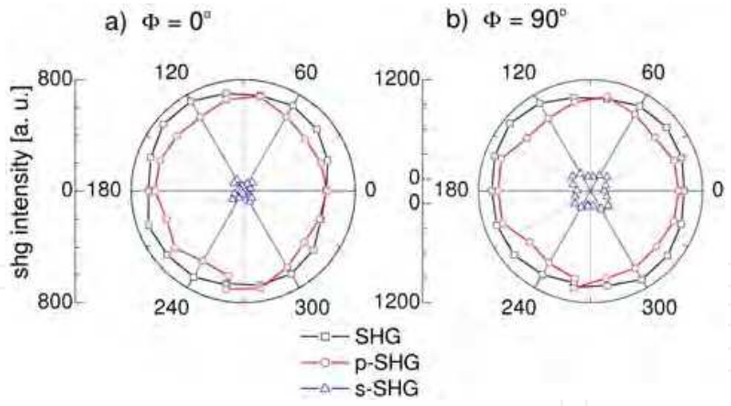

Fig. 14. SHG signal of spherical Ag NPs as a function of the polarization angle, α, obtained for two different sample orientations (see Figure 2): ϕ=0º (a) and ϕ=90º (b). In the plots, the total (opened squares, black), *p*-polarized (opened circles, red) and *s*-polarized (opened triangles, blue) SHG intensities are shown.

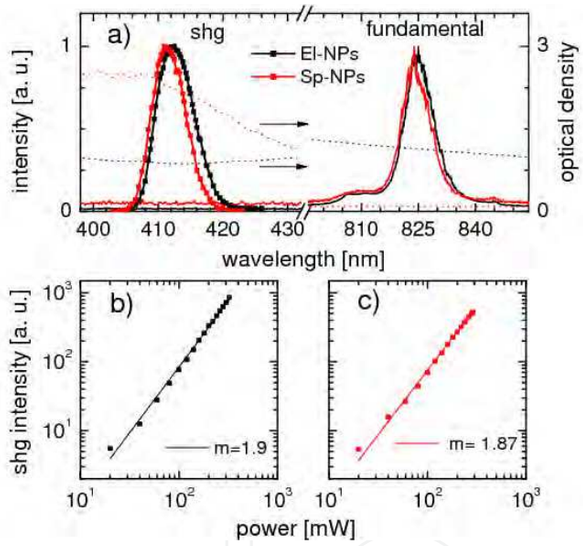

Fig. 15. (a) Fundamental laser spectra used in the SHG experiments and SHG spectra obtained for spherical and elongated NPs. In all plots, curves in black stands for elongated NPs while curves in red for spherical NPs. SHG signal as a function of the fundamental input power for elongated (b) and spherical (c) Ag-NPs, respectively. Here, solid squares denote the experimental data while continuous lines indicate the fitted curves. m: is the slope obtained from the linear fitting.

experiments are that this group obtained equivalent intensities for both *p*- and *s*-SH signal and no measurable signal for spherical NPs was detected. Their SH experiments were performed with the fundamental beam at an angle of incidence close to the surface normal, 15º (SH collected in transmission), and the NPs long axes aligned along the surface normal. We consider that such experimental arrangement is close to the case shown in Fig. 12a, since the direction of the fundamental beam is also close to the direction of the NPs long axis and comparable intensities are obtained for *p* and *s*-SH. As discussed above we believe that we

are able to detect SH from spherical NPs due to the fact that we have smaller NPs sizes (at least 10 times smaller) with respect to Podlipensky's samples. Note that Eqs. 8-9 do not explain this dependence, since they were obtained considering a hyperpolarizability tensor with cylindrical symmetry, however, it is interesting to note that our experimental results can be explained using analytical expressions obtained by Dadap *et. al.* (Dadap et al., 1999) to describe SH Rayleigh Scattering from spheres of centrosymmetric material, where the intensities for vertical and horizontal SH are given by $I_{p\alpha} \propto |a_1|^2$ and $I_{s\alpha} \propto |a_2|^2 \sin 2\alpha$, respectively. In these expressions, *p* and *s*, stands for the horizontal and vertical polarization of the harmonic generated signals, respectively, α, is the fundamental input polarization, and, a_1 and a_2, are complex numbers related to the pure effective dipole contribution and quadruple contribution, respectively. For *p*-SHG the intensity is constant, independent of the input polarization angle α, while for *s*-SHG intensity the signal is maximum at $\alpha = (2n\text{-}1)45°$ and vanishes at $\alpha = (n\text{-}1)90°$, with n =integer. Fig. 6b has been intentionally altered in order to see such *s*-SHG polar behavior. In addition, being the *p*-SH intensity higher with respect to the *s*-SH counterpart in our experiments (then $a_1 >> a_2$), strongly supports our assumption that the SHG is dominated by dipolar contributions arising from the surface of each non-perfectly spherical Ag-NP and having a quadratic response with respect to the input power (observed in Fig. 15c) confirms their coherent summation (Rocha-Mendoza et al., 2011).

6. Conclusions

The third-order nonlinear results here presented allows a better understanding of the nonlinear optical response of plasmonic nanocomposites, based on the electronic transitions occurred in the embedded NPs. For the studied wavelengths, the response depends on the incident irradiance, mainly because of the hot-electrons contribution. Regarding anisotropic plasmonic nanocomposites, for the wavelengths used in this work, the analysis may be done considering only one plasmon resonance at a time. This fact allows making the same considerations as for the isotropic case, and, for applications, by varying wavelength, polarization and angular position of the sample, one can switch the sign of the nonlinear optical response of these nanocomposites, which gives a wide picture of possible applications of these nanocomposites into the plasmonics realm.

Second-harmonic generation from composites containing randomly distributed but aligned elongated silver nanoparticles has been presented and modeled as a coherent summation of the microscopcic hyperpolarizability associated to each NP. Our experimental data suggest that the origin of the hyperpolarizability, in both elongated and spherical NPs, can be attributed mainly to a surface nonlinear contribution of each non-perfect ellipsoidal or spherical Ag-NP.

7. Acknowledgments

The authors wish to acknowledge the technical assistance of K. López, F. J. Jaimes, J. G. Morales and E. J. Robles-Raygoza. We would like to thank Dr. Eugenio Méndez for useful discussions. Finally, we also acknowledge the financial support from PAPIIT-UNAM through grants IN108510 and IN103609; from CONACyT through grants 80019 and 102937, from ICyT-DF through grant PICCT08-80, and (I. Rocha-Mendoza) from UC-MEXUS/CONACyT under collaborative research programs.

8. References

Aktsipetrov, O. A.; Elyutin, P. V.; Nikulin, A. A. & Ostrovskaya, E. A. (1995). Size effects in optical second-harmonic generation by metallic nanocrystals and semiconductor quantum dots: The role of quantum chaotic dynamics. *Phys. Rev. B*, 51, 17591–17599.

Bachelier, G.; Butet, J.; Russier-Antoine, I.; Jonin, C.; Benichou, E. & Brevet, P.-F. (2010). Origin of optical secondharmonic generation in spherical gold nanoparticles: Local surface and nonlocal bulk contributions. *Phys. Rev. B*, 82, 235403.

Barnes, W. L.; Dereux, A. & Ebbesen, T. W. (2003). Surface plasmon subwavelength optics. *Nature*, 424, 824–830.

Boyd, R. (2008). *Nonlinear optics* (3rd. Edition), Academic Press, USA.

Brevet, P-F. (2011) Second Harmonic Generation, *Comprehensive Nanoscience and Technology*, G. A. Wurtz, R.J. Pollard and A.V. Zayats, eds., 351–381, Elsevier.

Campagnola, P. J.; & Loew, L. M. (2003). Second-harmonic imaging microscopy for visualizing biomolecular arrays in cells, tissues and organisms. *Nature Biotech.*, 21, 1356–1360.

Dadap, J. I.; Shan, J.; Eisenthal, K. B. & Heinz, T. F. (1999). Second-Harmonic Rayleigh Scattering from a Sphere of Centrosymmetric Material. *Phys. Rev. Lett.*, 83, 4045–4048.

Dadap, J. I.; Shan, J. & Heinz, T. F. (2004). Theory of optical second-harmonic generation from a sphere of centrosymmetric material: small-particle limit. *J. Opt. Soc. Am. B*, 21, 1328-1347.

Fernández-Hernández, R. C.; Gleason-Villagrán, R.; Torres-Torres, C.; Cheang-Wong, J. C.; Crespo-Sosa, A.; Rodríguez-Fernández, L.; López-Suárez, A.; Rangel-Rojo, R.; L; Oliver, A. & Reyes-Esqueda, J. A. (2011). Nonlinear optical spectroscopy of isotropic and anisotropic metallic nanocomposites. *J. Phys.: Conference Series,* 274, 012074.

Figliozzi, P.; Sun, L.; Jiang, Y.; Matlis, N.; Mattern, B.; Downer, M. C.; Withrow, S. P.; White, C.W.; Mochán, W. L. & Mendoza, B. S. (2005). Single-Beam and Enhanced Two-beam second-harmonic generation from silicon nanocrystals by use of spatially inhomogeneous femtosecond pulses. *Phys. Rev. Lett.*, 94, 047401.

Freund, I.; Deutsch, M. & Sprecher, A. (1986). Connective tissue polarity. Optical second-harmonic microscopy, crossed-beam summation, and small-angle scattering in rat-tail tendon. *Biophys. J.*, 50, 693–712.

Gallet, S.; Verbiest, T. & Persoons, A. (2003). Second-order nonlinear optical properties of nanocrystalline maghemite particles. *Chem. Phys. Lett.*, 378, 101–104.

Hache, F.; Ricard, D. & Flytzanis, C. (1986). Optical nonlinearities of small metal particles: surface-mediated resonance and quantum size effects. *J. Opt. Soc. Am. B,* 3, 1647-1655.

Hache, F.; Ricard, D.; Flytzanis, C. & Kreibig, U. (1988). The optical kerr effect in small metal particles and metal colloids: the case of gold. *Appl. Phys. A: Mater. Sci. Process.,* 47, 347-357.

Hirose, C.; Akamatsu, N. & Domen, K. (1992). Formulas for the Analysis of the Surface SFG Spectrum and Transformation Coefficients of Cartesian SFG Tensor Components. *Appl. Spectrosc.*, 46, 1051–1072.

Inouye, H; Tanaka, K.; Tanahashi, I.; Hattori, T. & Nakatsuka, H. (2000). Ultrafast Optical Switching in a Silver Nanoparticle System. *JJAP,* 39, 5132–5133.

Karthikeyan, B.; Anija, M.; Suchand Sandeep, C. S.; Muhammad Nadeer, T. M. & Philip, R. (2008). Optical and nonlinear optical properties of copper nanocomposite glasses annealed near the glass softening temperature. *Opt. Commun.,* 281, 2933-2937.

Khosrofian, J. M. & Garetz, B. A. (1983). Measurement of a Gaussian laser beam diameter through the direct inversion of knife-edge data. *Appl. Opt.,* 22, 3406-3410.

Knoesen, A.; Sakalnis, S.; Wang, M.; Wise, W. D.; Lee, N. & Frank, C. W. (2004). Sum-frequency spectroscopy and imaging of aligned helical polypeptides. *IEEE J. Sel. Top. Quantum Electron.*, 10, 1154–1163.

Leray, A. ; Leroy, L. ; Le Grand, Y.; Odin, C. ; Renault, A.; Vi, V.; Roude, D.; Mallegol, T.; Mongin, O. ; Werts, M. H. V. & Blanchard-Desce, M. (2004). Organization and Orientation of Amphiphilic Push-Pull Chromophores Deposited in Langmuir-Blodgett Monolayers Studied by Second Harmonic Generation and Atomic Force Microscopy. *Langmuir*, 20, 8165–8171.

Liu, X.; Guo, S.; Wang, H. & Hou, L. (2001). Theoretical study on the closed aperture Z-scan curves in the materials with nonlinear refraction and strong nonlinear absortion. *Opt. Commun.*, 197, 431-437.

Matsui, I. (2005) Nanoparticles for Electronic Device Applications: A Brief Review, *JCEJ*, 38, 535–546.

McMahon, M. D.; Ferrara, D.; Bowie, C. T.; Lopez, R. & Haglund Jr., R. F. (2007). Second harmonic generation from resonantly excited arrays of gold nanoparticles. *Appl. Phys. B*, 87, 259–265.

Mendoza, B. S. & Mochán, W. L. (2006). Second harmonic surface response of a composite," *Opt. Mat.*, 29, 1–5.

Nappa, J.; Revillod, G.; Russier-Antoine, I.; Benichou, E.; Jonin, C. & Brevet, P-F. (2005). Electric dipole origin of the second harmonic generation of small metallic particles. *Phys. Rev. B*, 71, 165407.

Noguez, C. (2007). Surface plasmons on metal nanoparticles: the influence of shape and physical environment. *J. Phys. Chem. C,* 111, 3806-3819.

Oliver, A.; Reyes-Esqueda, J. A.; Cheang-Wong, J. C.; Román-Velázquez, C. E.; Crespo-Sosa, A.; Rodríguez-Fernández, L.; Seman, J. A. & Noguez, C. (2006). Controlled anisotropic deformation of Ag nanoparticles by Si ion irradiation. *Phys. Rev. B*, 74, 245425.

Podlipensky, A.; Lange, J.; Seifert, G.; Graener, H. & Cravetchi I. (2003). Second-harmonic generation from ellipsoidal silver nanoparticles embedded in silica glass. *Opt. Lett.* 28, 716–718.

Psilodimitrakopoulos, S.; Santos, S. I. C. O.; Amat-Roldan, I.; Thayil, A. K. N.; Artigas, D. & Loza-Alvarez, P. (2009). *In vivo*, pixel-resolution mapping of thick filaments' orientation in nonfibrilar muscle using polarization-sensitive second harmonic generation microscopy," *J. Biomed. Opt.,* 14, 014001.

Rangel-Rojo, R.; McCarthy, J.; Bookey, H. T.; Kar, A. K.; Rodríguez-Fernández, L.; Cheang-Wong, J. C.; Crespo-Sosa, A.; Lopez-Suarez, A.; Oliver, A.; Rodríguez-Iglesias, V. & Silva-Pereyra, H. G. (2009). Anisotropy in the nonlinear absorption of elongated silver nanoparticles in silica, probed by femtosecond pulses. *Opt. Commun.*, 282, 1909–1912.

Rangel-Rojo, R; Reyes-Esqueda, J. A.; Torres-Torres, C.; Oliver, A.; Rodríguez-Fernández, L.; Crespo-Sosa, A.; Cheang-Wong, J. C.; McCarthy, J.; Bookey, H. T. & Kar, A. K. (2010). Linear and nonlinear optical properties of aligned elongated silver nanoparticles embedded in silica, In: *Silver Nanoparticles*, David Pozo Perez eds., 35–62, InTech, http://www.intechopen.com/articles/show/title/linear-and-nonlinear-optical-propertiesof-aligned-elongated-silver-nanoparticles-embedded-in-silica.

Reyes-Esqueda, J. A.; Torres-Torres, C.; Cheang-Wong, J. C.; Crespo-Sosa, A.; Rodríguez-Fernández, L.; Noguez, C. & Oliver, A. (2008). Large optical birefringence by anisotropic silver nanocomposites. *Optics Express,* 16, 710-717.

Reyes-Esqueda, J. A.; Rodríguez-Iglesias, V.; Silva-Pereyra, H. G.; Torres-Torres, C.; Santiago-Ramírez, A.-L.; Cheang-Wong, J. C.; Crespo-Sosa, A.; Rodríguez-

Fernández, L.; López-Suárez, A. & Oliver, A. (2009). Anisotropic linear and nonlinear optical properties from anisotropy-controlled metallic nanocomposites. *Optics Express,* 17, 12849-12868.

Rocha-Mendoza, I.; Yankelevich, D. R.; Wang, M.; Reiser, K. M.; Frank, C. W. & Knoesen, A. (2007). Sum Frequency Vibrational Spectroscopy: The Molecular Origins of the Optical Second-Order Nonlinearity of Collagen. *Biophys. J.*, 93, 4433–4444.

Rocha-Mendoza, I; Rangel-Rojo, R.; Oliver, A. & Rodríguez-Fernández, L. (2011). Second-order nonlinear response of composites containing aligned elongated silver nanoparticles. *Optics Express* 19, 21575-21587.

Rodríguez-Iglesias, V.; Silva-Pereyra, H. G.; Cheang-Wong, J. C.; Reyes-Esqueda, J. A.; Rodríguez-Fernández, L.; Crespo-Sosa, A.; Kellerman, G. & Oliver, A. (2008). MeV Si ion irradiation effects on the optical absorption properties of metallic nanoparticles embedded in silica. *Nuc. Instrum. Meth. B*, 266, 3138-3142.

Rodríguez-Iglesias, V.; Silva-Pereyra, H. G.; Torres-Torres, C.; Reyes-Esqueda, J. A.; Cheang-Wong, J. C.; Crespo-Sosa, A.; Rodríguez-Fernández, L.; López-Suárez, A. & Oliver, A. (2009). Large and anisotropic third-order nonlinear optical response from anisotropy-controlled metallic nanocomposites. *Opt. Commun.,* 282, 4157-4161.

Ryasnyansky, A.; Palpant, B.; Debrus, S.; Khaibullin, R. I. & Stepanov, A. L. (2006). Nonlinear optical properties of copper nanoparticles synthesized in indium tin oxide matrix by ion implantation. *J. Opt. Soc. Am. B,* 23, 1348-1353.

Sheik-Bahae, M.; Said, A. A.; Wei, T. H. & van Stryland, E. W. (1990). Sensitive Measurement of Optical Nonlinearities Using a Single Beam. *IEEE J. Quant. Electron.,* 26, 760-769.

Shen, Y. R. (1989). Surface properties probed by second-harmonic and sum-frequency generation. *Nature*, 337, 519–525.

Silva-Pereyra, H. G.; Arenas-Alatorre, J.; Rodríguez-Fernández, L.; Crespo-Sosa, A.; Cheang-Wong, J. C.; Reyes-Esqueda, J. A. & Oliver, A. (2010). High stability of the crystalline configuration of Au nanoparticles embedded in silica under ion and electron irradiation. *J. Nanopart. Res.,* 12, 1787-1795.

Stoller, P.; Celliers, P. M.; Reiser, K. M. & Rubenchik, A. M. (2003). Quantitative second-harmonic generation microscopy in collagen. *Appl. Opt.,* Vol. 42, No. 25, 5209–5219.

Tominaga, J.; Mihalcea, C.; Buchel, D.; Fukuda, H.; Nakano, T.; Atoda, N.; Fuji, H. & Kikukawa, T. (2001). Local plasmon photonic transistor. *Appl. Phys. Lett.,* 78, 2417–2419.

Torres-Torres, C.; Reyes-Esqueda, J. A.; Cheang-Wong, J. C.; Crespo-Sosa, A.; Rodríguez-Fernández, L & Oliver, A. (2008). Optical third-order nonlinearity by nanosecond and picosecond pulses in Cu nanoparticles in ion-implanted silica. *J. Appl. Phys.,* 104, 014306.

Valencia, C. I.; Méndez, E. R. & Mendoza, B. S. (2004). Second-harmonic generation in the scattering of light by an infinite cylinder. *J. Opt. Soc. Am. B*, 21, 36–44.

Valencia, C. I.; Méndez, E. R. & Mendoza, B. S. (2009). Weak localization effects in the second-harmonic light scattered by random systems of particles. *Opt. Commun.*, 282, 1706–1709.

Wang, K.; Long, H.; Fu, M.; Yang, G. & Lu, P. (2010). Size-related third order optical nonlinearities of Au nanoparticle arrays. *Optics Express,* 18, 13874-13879.

Zheludev, N. I. & Emelyanov, V. I. (2004). Phase matched second harmonic generation from nanostructured metallic surfaces. *J. Opt. A: Pure App. Opt.,* 6, 26-28.

Zhuang, X.; Miranda, P. B.; Kim, D. & Shen, Y. R. (1999). Mapping molecular orientation and conformation at interfaces by surface nonlinear optics. *Phys. Rev. B*, 59, 12632–12640.

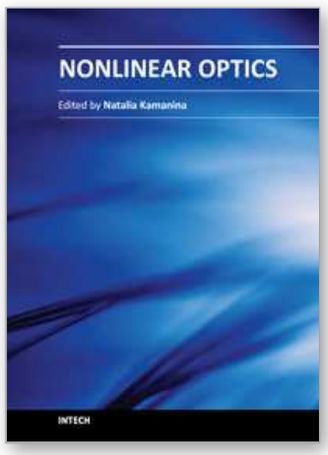

Nonlinear Optics

Edited by Dr. Natalia Kamanina

ISBN 978-953-51-0131-4
Hard cover, 224 pages
Publisher InTech
Published online 29, February, 2012
Published in print edition February, 2012

Rapid development of optoelectronic devices and laser techniques poses an important task of creating and studying, from one side, the structures capable of effectively converting, modulating, and recording optical data in a wide range of radiation energy densities and frequencies, from another side, the new schemes and approaches capable to activate and simulate the modern features. It is well known that nonlinear optical phenomena and nonlinear optical materials have the promising place to resolve these complicated technical tasks. The advanced idea, approach, and information described in this book will be fruitful for the readers to find a sustainable solution in a fundamental study and in the industry approach. The book can be useful for the students, post-graduate students, engineers, researchers and technical officers of optoelectronic universities and companies.

InTech Europe
University Campus STeP Ri
Slavka Krautzeka 83/A
51000 Rijeka, Croatia
Phone: +385 (51) 770 447
Fax: +385 (51) 686 166
www.intechopen.com

InTech China
Unit 405, Office Block, Hotel Equatorial Shanghai
No.65, Yan An Road (West), Shanghai, 200040, China
中国上海市延安西路65号上海国际贵都大饭店办公楼405单元
Phone: +86-21-62489820
Fax: +86-21-62489821

IntechOpen